INT. J. NUM. METH. HEAT FLUID FLOW, VOL. 3, 429–444 (1993)

FINITE ELEMENT ANALYSIS OF TWO DIMENSIONAL RAYLEIGH–BENARD CONVECTION WITH GRAVITY MODULATION EFFECTS*

BALASUBRAMANIAM RAMASWAMY

Department of Mechanical Engineering and Materials Science, Rice University, PO Box 1892, Houston, Texas 77251-1892, USA

ABSTRACT

Sinusoidal gravity modulation fields imposed on two-dimensional Rayleigh–Benard convection flow are studied to understand the effects of periodic source (g-jitter) on fluids system and heat transfer mechanism. The transient Navier–Stokes and energy equations are solved by semi-implicit operator splitting finite element method. Results include two sets. One is considered at normal terrestrial condition and the other one is related to low-gravity condition. Under low-gravity condition the research focuses on the effects of modulation frequency and direction in order to find out the critical frequency for heat transfer mechanism transferring from conduction to convection.

KEY WORDS Rayleigh–Benard convection Gravity modulation

INTRODUCTION

Benard convection occurring in modulated gravitational fields has been of great interest because of the induced change in the stability bounds and its practical applications. A quiescent fluid layer heated uniformly from below will develop an unstable convection flow caused by the adverse density distribution at a Rayleigh number greater than some critical value. A sinusoidal gravity modulation (g-jitter) under certain combinations of the flow parameters may stabilize this phenomenon[1]. Similarly, a static stable fluid heated from above may be destabilized by a sinusoidal gravity modulation at certain flow field conditions. According to the literature[2,3], the sinusoidal modulated temperature field can influence the convective flow characteristics; and the interaction between the sinusoidal modulated temperature field and the gravitational field may generate a mean steady flow. Recently, Wheeler *et al.*[4] investigated the stability of this problem in high frequency gravity modulation.

The concern over the strong natural convection adversely affecting materials processing under a low-gravity environment such as space lab is becoming more and more important. In these space environments, there are a lot of perturbations created by mechanical vibrations, solar drag, crew activities and orbiter maneuvres, etc. They can have a serious effect on the flow field at low gravity status. Following the study by Knabe and Eilers[5], the maximum vibration amplitude of these motions is of order 10^{-2}–$10^{-3}g_0$ where g_0 is the terrestrial gravity; and these disturbances become important since the orbital gravity is also small compared to g_0. Therefore,

* This research was sponsored by National Science Foundation under grant DMS-9112847.

0961–5539/93/050429–16$2.00

Received August 1992
Revised April 1993

the investigation of the g-jitter effect in a low-gravity environment is interesting and important in practical applications. A summary of the related work directed towards high-frequency vibration at zero-g level is also available in Gershuni's research[6]. The main objective of this work is to simulate a liquid metal fluid in low-gravity environments. A parametric study is conducted to determine the critical modulation frequency for both vertical and horizontal modulations.

A two-dimensional rectangular cavity with aspect ratio 0.5 is set as the physical domain. All the numerical results demonstrate an agreement with the previous literature[1,7,8].

STATEMENT OF THE PROBLEM

In this problem, the transient 2-D incompressible Navier–Stokes and energy equations are considered. These equations are non-dimensionalized, using the width of the cavity L as the length scale, $\rho\alpha^2/L^2$ as the pressure scale and L^2/α, α/L as the thermal diffusion time and velocity scale, respectively, ρ and α are the density and thermal diffusivity of the fluid, respectively. The temperature is non-dimensionalized by using the ratio $(T^* - T_m^*)/(T_h^* - T_c^*)$ where T_h^* and T_c^* represent the hot wall and cold wall temperatures, respectively, and T_m^* is the mean temperature in the cavity. Applying these scales, the non-dimensionalized equations are written as:

Continuity:

$$\frac{\partial u}{\partial x} + \frac{\partial v}{\partial y} = 0 \tag{1}$$

x-*momentum:*

$$\frac{\partial u}{\partial t} + \left(u\frac{\partial u}{\partial x} + v\frac{\partial u}{\partial y}\right) = -\frac{\partial p}{\partial x} + Pr\left(\frac{\partial^2 u}{\partial x^2} + \frac{\partial^2 u}{\partial y^2}\right) + S_1 \tag{2}$$

y-*momentum:*

$$\frac{\partial v}{\partial t} + \left(u\frac{\partial v}{\partial x} + v\frac{\partial v}{\partial y}\right) = -\frac{\partial p}{\partial y} + Pr\left(\frac{\partial^2 v}{\partial x^2} + \frac{\partial^2 v}{\partial y^2}\right) + S_2 \tag{3}$$

Energy:

$$\frac{\partial \theta}{\partial t} + \left(u\frac{\partial \theta}{\partial x} + v\frac{\partial \theta}{\partial y}\right) = \left(\frac{\partial^2 \theta}{\partial x^2} + \frac{\partial^2 \theta}{\partial y^2}\right) \tag{4}$$

where:

$$S_1 = S_2 = RaPr\theta[F_m + \eta\cos(\omega t + \bar{\phi})] \tag{5}$$

Here u and v are velocities along the x and y directions, respectively, and θ, p and t are temperature, pressure and time, respectively. These equations represent the unsteady, laminar flow with Boussinesq approximation for the buoyancy effect. Depending on the application of gravity modulation direction, one of the source terms (either S_1 or S_2) is set equal to zero. F_m and η in (5) represent the constant mean gravity level and maximum gravity oscillation amplitude, respectively. The $\bar{\phi}$ stands for random phase angle, which is set equal to zero for sinusoidal oscillation. The dimensionless parameters appearing in the equations include the non-dimensionalized frequency ω defined as $\omega = \bar{\Omega}L^2/\alpha$ where $\bar{\Omega}$ is the dimensional frequency, the Prandtl number $Pr = \nu/\alpha$ where ν is the kinematic viscosity, and the Rayleigh number $Ra = [g\beta L^3(T_h^* - T_c^*)]/\alpha\nu$ where g and β stands for the gravitational constant, and thermal expansion ratio, respectively.

Because the governing equations are two-dimensional and time-dependent, a set of proper boundary conditions and initial conditions is necessary. Following the physical problem

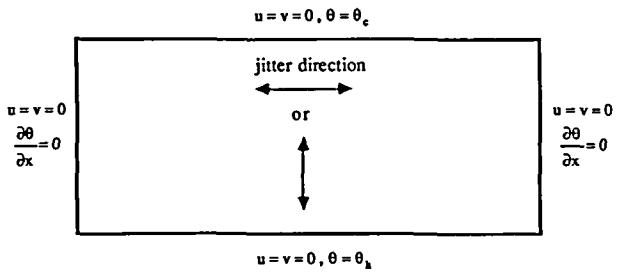

Figure 1 Problem definition of Benard convection with gravity modulation effect

definition, the boundary conditions are written as (see *Figure 1*):

$$u = v = 0, \qquad \theta = \theta_h = 0.5, \qquad (y = 0) \tag{6}$$

$$u = v = 0, \qquad \theta = \theta_c = -0.5, \qquad (y = H/L) \tag{7}$$

$$u = v = 0, \qquad \frac{\partial \theta}{\partial x} = 0, \qquad (x = 0) \text{ and } (x = 1) \tag{8}$$

METHOD OF SOLUTION

We presented the finite element formulation used in detail in our previous work[9,10]. Here we summarize briefly the major ingredients of the formulation and resulting equations, and point out some important features regarding the practical application of these equations. The continuous domain Ω is divided into non-overlapping 4-noded bilinear quadrilateral elements. Thus the unknown variables u, v, p, and θ, are approximated by bilinear interpolation functions in each local finite element as:

$$u = \Phi_\alpha u_\alpha$$

$$v = \Phi_\alpha v_\alpha$$

$$p = \Phi_\alpha p_\alpha$$

$$\theta = \Phi_\alpha \theta_\alpha$$

The Galerkin finite element method is used for spatial discretization. A semi-implicit time-splitting scheme is used for the temporal discretization. The solution procedure of the system is accomplished by splitting the equation into parts: the non-linear terms are advanced by the explicit second order Adams–Bashforth scheme, and the linear diffusion terms are advanced by an implicit Euler scheme.

Step 1

At the first step, a set of equations is solved without inclusion of the pressure term:

$$\frac{\tilde{\mathbf{u}}^{n+1} - \mathbf{u}^n}{\Delta t} = -[\tfrac{3}{2}(\mathbf{u}\cdot\nabla\mathbf{u})^n - \tfrac{1}{2}(\mathbf{u}\cdot\nabla\mathbf{u})^{n-1}] + Pr\nabla\cdot\nabla\mathbf{u}^{n+1} + \mathbf{n}_g S^n \tag{9}$$

where $\mathbf{n}_g$ is the unit vector along the gravity direction. After this intermediate step, the flow field is not incompressible.

Step 2

The pressure is then used to enforce incompressibility. A Poisson equation for the pressure is obtained by taking the divergence of the momentum equation. Assume that $\mathbf{u}^{n+1}$ is

incompressible, the equation for the pressure is:

$$\nabla^2 \mathbf{p}^{n+1} = \frac{1}{\Delta t} \nabla \cdot \tilde{\mathbf{u}}^{n+1} \tag{10}$$

Using the intermediate velocity $\tilde{\mathbf{u}}$ and pressure p, we correct the final velocity as:

$$\mathbf{u}^{n+1} = \tilde{\mathbf{u}}^{n+1} - \Delta t \nabla \mathbf{p}^{n+1} \tag{11}$$

Step 3

A similar procedure is used for the temperature calculation θ^{n+1} by solving the energy equation:

$$\frac{\theta^{n+1} - \theta^n}{\Delta t} = -[\tfrac{3}{2}(\mathbf{u} \cdot \nabla \theta)^n - \tfrac{1}{2}(\mathbf{u} \cdot \nabla \theta)^{n-1}] + \nabla \cdot \nabla \theta^{n+1} \tag{12}$$

When the finite element approximation is applied to (9)–(12) by the Galerkin method, it yields non-linear simultaneous ordinary differential equations of the form:

for Step 1:

$$M(\tilde{\mathbf{u}}^{n+1} - \mathbf{u}^n)/\Delta t = -[\tfrac{3}{2}K(\mathbf{u}^n)\mathbf{u}^n - \tfrac{1}{2}K(\mathbf{u}^{n-1})\mathbf{u}^{n-1}] - PrS(\tilde{\mathbf{u}}^{n+1}) + F_1^{n+1} \tag{13}$$

where M is the consistent mass matrix, K the advection matrix, S the diffusion matrix, and F_1 results from the imposition of natural boundary conditions and the exertion of a body force. The essential boundary conditions for the velocity field are imposed in this step. The convective terms are treated explicitly and the viscous terms are treated implicitly making this procedure semi-implicit.

for Step 2:

The spatially discrete form of problem (10) and (11) is:

$$Ap^{n+1} = -\frac{1}{\Delta t} D\tilde{\mathbf{u}}^{n+1} \tag{14}$$

$$M(\mathbf{u}^{n+1} - \tilde{\mathbf{u}}^{n+1})/\Delta t - Cp^{n+1} = 0 \tag{15}$$

$$D\mathbf{u}^{n+1} = 0 \tag{16}$$

where A, C and D are Laplacian, pressure gradient and divergence matrices, respectively. The Poisson equation system for the pressure is computed only once, is assembled, modified for the pressure boundary conditions, and factored (only once). Then at each time step, or iteration, it is only necessary to perform a forward and backward substitution to obtain the pressure.

for Step 3:

The spatially discrete form of problem (12) is:

$$M(\theta^{n+1} - \theta^n)/\Delta t = -[\tfrac{3}{2}K(\mathbf{u}^n)\theta^n - \tfrac{1}{2}K(\mathbf{u}^{n-1})\theta^{n-1}] - S(\theta^{n+1}) + F_2^{n+1} \tag{17}$$

where F_2 results from the natural boundary condition. The essential boundary conditions for the temperature field is imposed in this step.

RESULTS AND DISCUSSION

All the numerical results were calculated with zero initial velocity, pressure and temperature field. In consideration of computational cost and accuracy by observing *Table 1*, the results we obtained are calculated by uniform meshes 20 × 40, 20 × 60 and 20 × 80 for aspect ratios 0.5, 0.33, and 0.25, respectively. According to the periodic phenomena of the results with g-jitter effect, a time step is determined by defining each period including how many time steps. A fewer time steps per period are used in earlier stage; then more steps per period are used to calculate

Table 1 Influence of finite element mesh on the solution

	$Ra = 4500$, $\omega = 1400$ $\eta = 19.6$ (vertical jitter)			$Ra = 4500$, $\omega = 1400$ $\eta = 19.6$ (horizontal jitter)			$\omega = 45.5$, zero-g (vertical jitter)			$\omega = 200$, zero-g (horizontal jitter)		
Mesh	Nu_h	Nu_c	Max. $\|\Psi\|$	Nu_h	Nu_c	Max. $\|\Psi\|$	Nu_h	Nu_c	Max. $\|\Psi\|$	Nu_h	Nu_c	Max. $\|\Psi\|$
15 × 30	1.958	1.958	0.0277	4.127	4.127	8.33	2.000	2.000	0.0302	2.004	2.004	0.205
20 × 40	1.968	1.968	0.0288	4.200	4.200	8.53	2.000	2.000	0.0244	2.005	2.005	0.245
20 × 50	1.975	1.975	0.0292	4.240	4.240	8.53	2.000	2.000	0.0206	2.005	2.005	0.262

Table 2 Influence of time step on the solution (calculated by 25 × 50 mesh)

	$Ra = 4500$, $\omega = 1400$ $\eta = 19.6$ (vertical jitter)			$Ra = 4500$, $\omega = 1400$ $\eta = 19.6$ (horizontal jitter)		
Time steps per period	Nu_h	Nu_c	Max. $\|\Psi\|$	Nu_h	Nu_c	Max. $\|\Psi\|$
50	1.976	1.976	0.0233	4.248	4.248	8.57
100	1.975	1.975	0.0292	4.240	4.240	8.53
150	1.974	1.974	0.0344	4.225	4.225	8.46

the time-averaged results. Usually, the first value is chosen as 50 for most of the results and the second value is set 100. The relative difference in global and local properties between time steps is small for convective results. For conductive type results in normal gravity environment, the difference in local properties is big, but the global properties are retained the same. The results for different time steps in normal gravity state are listed in *Table 2*.

The results presented and discussed in this section are in two parts. The first one is concerned with the effect of gravity modulation in one-g terrestrial environment. The second part contains the non-linear analyses of the zero-gravity cases.

*Results at terrestrial one-*g *gravity.* We consider a cavity fluid heated from above or below with a sinusoidally modulated gravity modulational field. Before discussing the gravity modulation cases, we chose a few Benard convection cases to serve as benchmark references for understanding the history of the development of convection flow and the evolution of physical phenomena. Both of the onset of convection cells and the subsequent dynamics are described. The Rayleigh–Benard instability is triggered by heating the lower horizontal plate. In *Figure 2* we show an example for a subcritical Rayleigh number $Ra = 1600$ and aspect ratio 0.5. There are four circulations symmetrically existing in the cavity and a conductive type isotherms which is linear distribution along the height of cavity. Because the system is heated at the Rayleigh number below the critical value, the flow will always keep in stable status. The physical mechanism responsible for the situation is due to the balance between the lower cells and the upper cells. The fluid particles in the lower cells release energy by moving up and the fluid particles in upper cells receiving energy in falling period[11]. Due to the insulating side walls effect, the particles move from the side walls to centre and go up or down and the status achieves balance at the centreline. The maintenance of this balance status strongly depends on the viscosity of fluid, temperature difference between top and bottom walls, the consequent expansion of fluid and gravitational acceleration. All of these factors are included in the dimensionless parameter Ra. Therefore, the Rayleigh number is chosen as an index for the stability of Rayleigh–Benard convection. In the next example, the results correspond to a Rayleigh number $Ra = 4500$ greater than the critical value. As the stable case, the flow contains four cells in the domain in the earlier period. Later this state will be broken owing to the higher Rayleigh number, and the lower cells

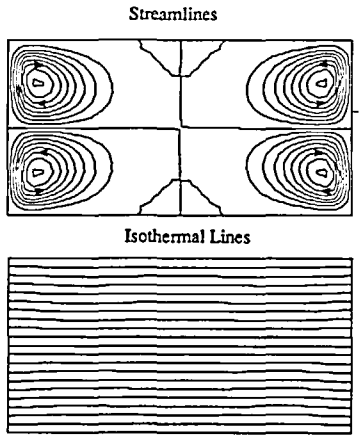

Figure 2 Streamlines and isotherms for $Ra = 1600$, $Pr = 7$, $Ar = 0.5$, one-g (no jitter)

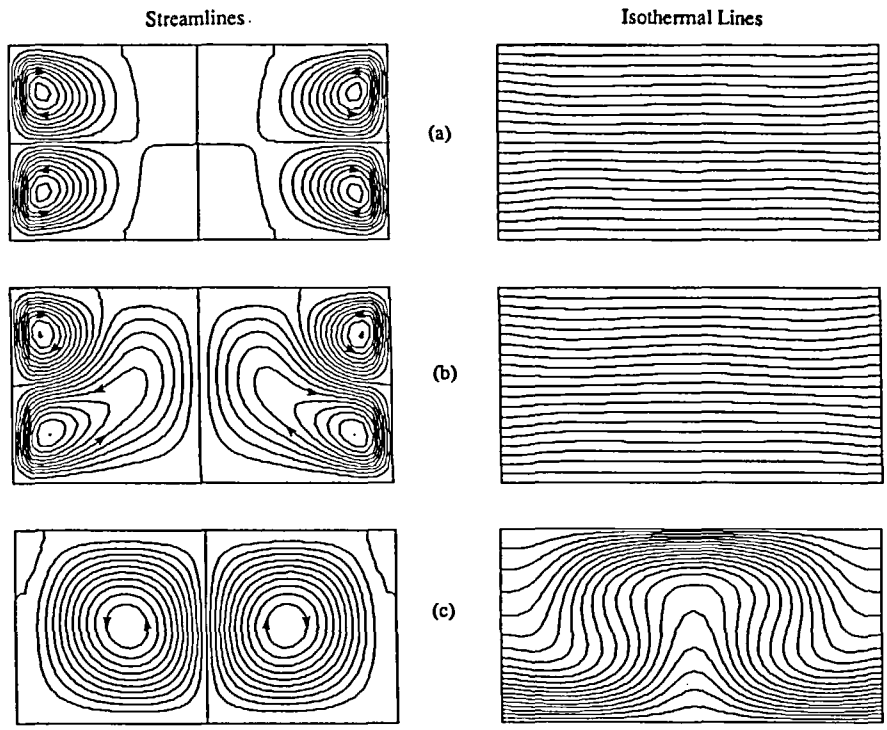

Figure 3 Streamlines and isotherms for $Ra = 4500$, $Pr = 7$, $Ar = 0.5$, one-g (no jitter): (a) $t = 0.05$ sec; (b) $t = 0.425$ sec; (c) $t = 1.5$ sec

or upper cells are going to develop and force the other cells to shrink. In this case, the lower cells move up from the centre and expand size (see *Figures 3a* and *b*). At $t = 1.5$ the pattern shown in *Figure 3c* has fully developed. The strong convective flow makes the isotherms change from conductive type to convective type. Actually, the relation between convection flow and temperature distribution has mutual influence. Although the flow influences the temperature distribution, the temperature gradient with a component which is orthogonal to the gravitational

field will enforce the circulation. Following the interaction, the flow finally developed a complete convective flow field. According to Gresho and Sani[1], at this Rayleigh number, a modulation amplitude of $\eta = 19.6$ and modulation frequency of $\omega = 1500$ will stabilize this flow when gravity and temperature gradient are acting along the same direction. The results obtained by using these parameters are displayed in *Figure 4a*. The main circulations change from two to four with two secondary circulations in each one and the magnitude of stream function becomes weaker when compared to the case with $\eta = 0$. Due to the g-jitter stabilizing the flow field, the heat transfer mechanism is conductive and not convective as it is in the no g-jitter case (see *Figure 3c*). Next, a random modulation example is investigated for the simulation of typical

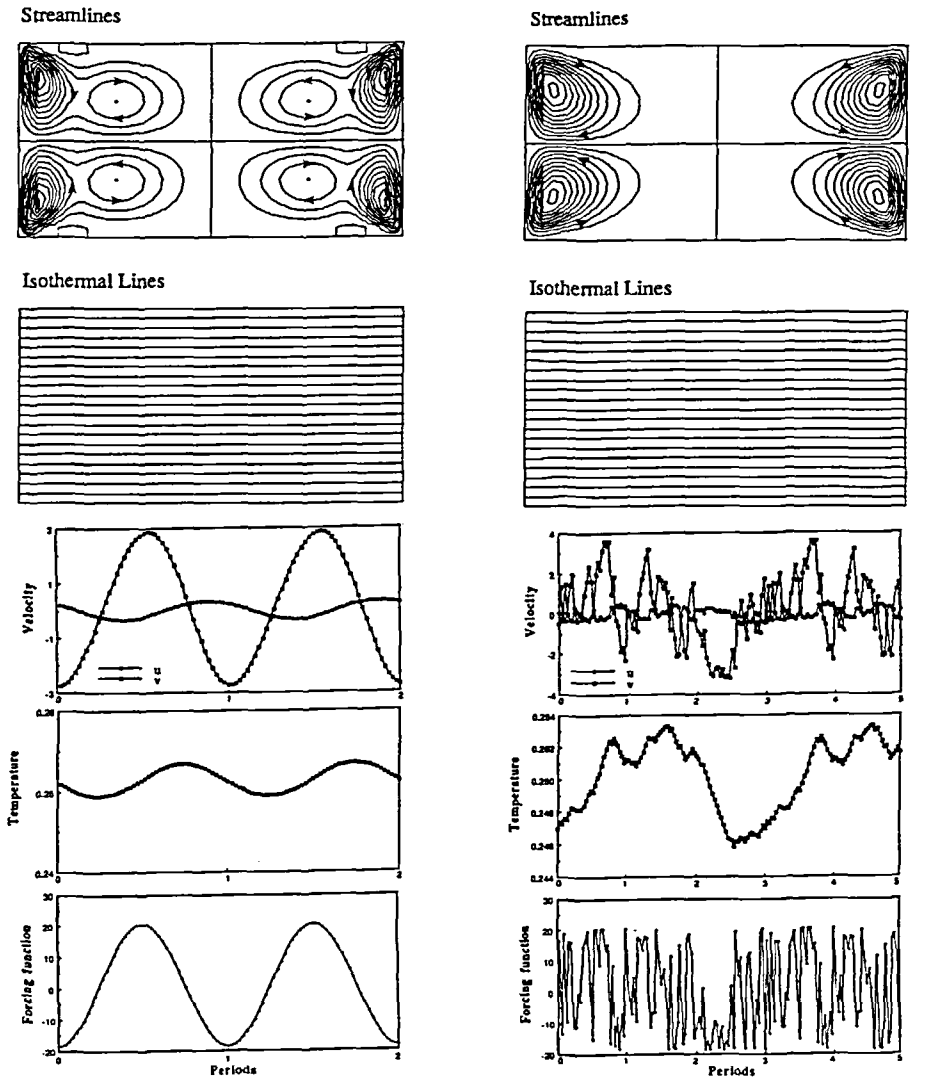

Figure 4 Time-averaged results for $Ra = 4500$, $Pr = 7$, $\eta = 19.6$, $\omega = 1400$, $Ar = 0.5$; (a) one-g (vertical jitter), ($\Psi_{max} = 0.0288$, $\Psi_{min} = -0.0288$, 19 contour lines), ($\theta_{max} = 0.5$, $\theta_{min} = -0.5$, 21 contour lines); (b) one-g random modulation (vertical jitter), ($\Psi_{max} = 0.0012$, $\Psi_{min} = -0.0012$, 19 contour lines), ($\theta_{max} = 0.5$, $\theta_{min} = -0.5$, 21 contour lines)

environment with the above parameters. A temporal random phase angle is induced in the source term between 0 and 2π. The time-averaged results display in *Figure 4b* show four counter-rotating vortices of higher intensity than the periodic case shown in *Figure 4a*. The time-averaged temperature contours demonstrate a weak convective nature of the flow. Compared with the sinusoidal modulation results, the random modulation is more marginally excitatory with the same maximum amplitude. An extensive study for normal terrestrial conditions, that is for one-g gravity, is given elsewhere[10]. *Table 3* shows the comparison of maximum stream function value with the results reported by Danabasoglu and Biringen[7] for different amplitudes and directions. A close agreement can be seen.

In the cases of smaller aspect ratios, more cells are subsequently created in the cavity with $\eta = 0$. The history of circulation development is an important information for understanding the final results. In earlier period, similarly it is a two-layer cellular pattern as in *Figure 5a* for $Ra = 3000$, $Ar = 0.25$. The circulation in the central portion are weaker than the cells far from the centre. If the flow is unstable, the central portion balance state will disappear and one of the two layers is going to develop stronger. After the circulation in the central portion becomes more and more strong, the shear flow effect resulting from the central circulation will force the cells next to it to become unstable. Basically, the flow is symmetric, so the circulations are symmetrically distributed in the domain as in *Figure 5*. Similar symmetric results are existed in the $Ar = 0.33$ case. The results shown in *Figure 6* are results for $Ra = 3000$ and $Ar = 0.33$. But these symmetric situations are easily to be disturbed by perturbation and are altered to other patterns. In this study, we applied a perturbation as used by Goldirsh *et al.*[12] $\delta\theta = A_m \exp[-((x - x_0)^2 + (y - y_0)^2)/C$ with $A_m = 0.01$, $(x_0, y_0) = (0.25, 0.25)$ and $C = 1$ for 0.5 sec, then removed the perturbation. The final results are shown in *Figure 6f* and the results cannot go back to the original pattern as shown in *Figure 6e*. According to literature some

Table 3 Comparison of maximum stream function value (calculated by 20 × 40 mesh and 100 time steps per period)

$Ra = 4500$, $\omega = 1400$	Present method	Danabasoglu and Biringen[7]
$\eta = 19.6$ (vertical jitter)	0.0288	0.0292
$\eta = 0.1$ (vertical jitter)	4.37	4.57
$\eta = 19.6$ (horizontal jitter)	8.53	8.76
$\eta = 0.1$ (horizontal jitter)	6.30	6.49

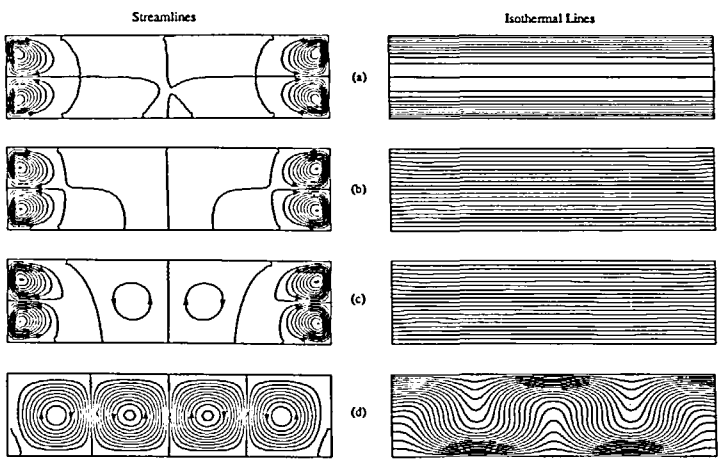

Figure 5 Streamlines and isotherms for $Ra = 3000$, $Pr = 7$, $Ar = 0.25$, one-g (no jitter): (a) $t = 0.02$ sec; (b) $t = 0.3$ sec; (c) $t = 0.5$ sec; (d) $t = 2.0$ sec

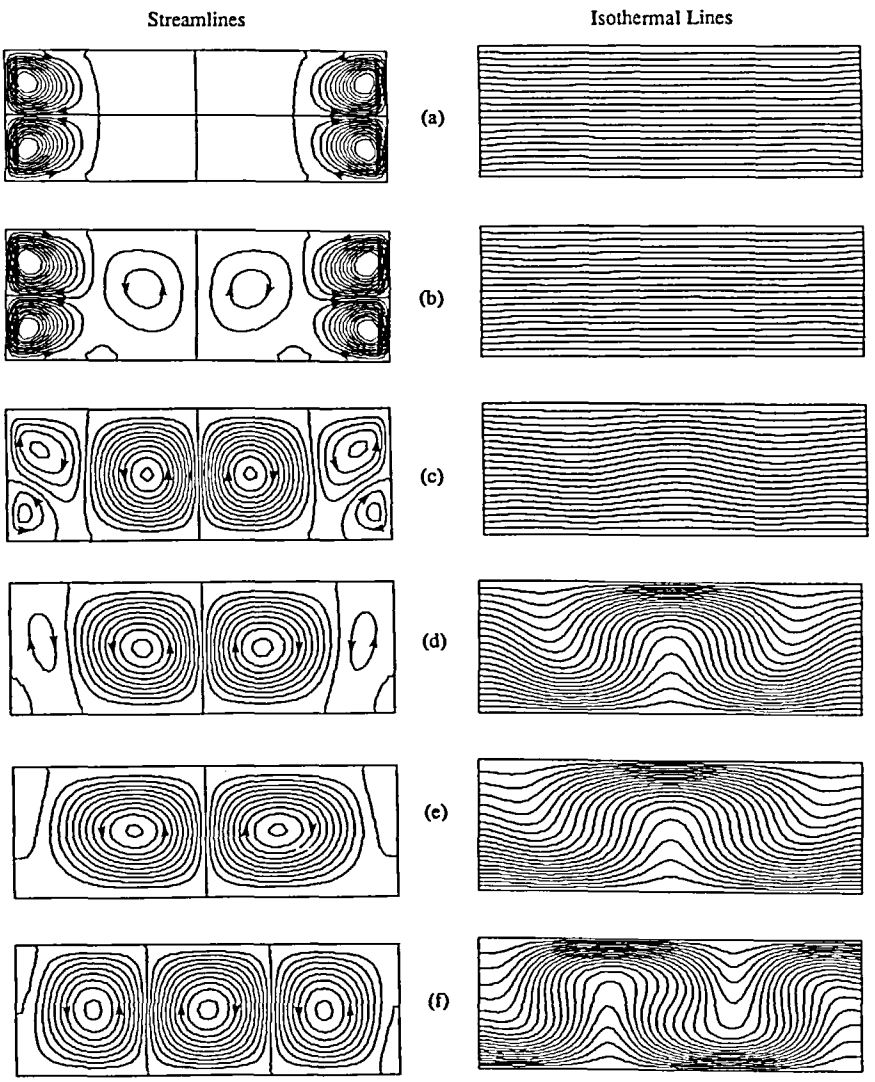

Figure 6 Streamlines and isotherms for $Ra = 3000$, $Pr = 7$, $Ar = 0.33$, one-g (no jitter): (a) $t = 0.1$ sec; (b) $t = 1.5$ sec; (c) $t = 1.7$ sec; (d) $t = 2.5$ sec; (e) $t = 6.0$ sec; (f) with perturbation

workers[12–14] solutions obtained in this research are in good agreement with their physical description.

Results at zero-gravity environment. The focus is put on the effects of gravity modulation and direction in a zero-gravity environment. According to the practical applications, a low Prandtl number material, such as liquid metal, is a typical sample for investigating flow field and heat transfer in the zero-gravity environment. In these calculations, we set the thermal diffusivity $\alpha = 2.2 \times 10^{-5}\ \mathrm{m^2/sec}$, kinematic viscosity $\nu = 1.54 \times 10^{-7}\ \mathrm{m^2/sec}$ and thermal expansion $\beta = 10^{-4}\ \mathrm{K^{-1}}$ as the liquid metal material properties. When the flow field exists in a g-jitter environment with maximum amplitude $10^{-3}g$, characteristic length 18 cm and maximum temperature difference 100 K, we calculated the Prandtl number $Pr = 7 \times 10^{-3}$ and Rayleigh number $Ra = 1.771 \times 10^5$ by applying these values and the material properties. The purpose for the study in zero-gravity is to investigate the modulation direction and frequency influence,

so the Prandtl number and Rayleigh number are fixed to the above values for all the calculations in this section to make the comparison easy.

In the first set of computations, the cavity was subjected to vertical gravity modulation along the direction of the temperature gradient, and a different modulation frequency was chosen for each case to find the critical value for the heat transfer mechanism changing from conduction to convection. We started with a high frequency $\omega = 4543$ case and chose $\eta = 1$. That means that the maximum modulation amplitude $10^{-3}g$ is included in the Rayleigh number calculation. The results are shown in *Figure 7*. The streamlines include four primary calculations (lower left and upper right circulations in counterclockwise direction, and lower right and upper left circulations in clockwise direction) with a counter-rotating small circulation at each corner of the cavity and the temperature contours display a conductive pattern. The point data history, owing to the small modulation, demonstrates a small variation; and the temperature data contour is close to a straight line. In addition, the low Prandtl number results in the physical phenomena changing slowly and taking much more computational time than the terrestrial cases.

In the subsequent case presented here, the ω is reduced to 200 in order to investigate the effect of the frequency. *Figure 8* includes the time-averaged streamlines, isotherms along with the point data history. The streamlines show eight primary circulations existing which means that the circulations developing from the small circulations in the previous case have become stronger. As ω is continuously reduced to 45.5, the fluid domain contains only four circulations (see *Figure 9*) which are the circulations developing from the small circulations which stay at corners as shown in *Figure 7* and dominating the fluid flow field. The heat transfer mechanism is still conductive, so point data history of temperature remains a straight line. The velocity variation is a synchronous response and the flow field is still unexcited.

When the frequency is reduced to 20, the physical phenomena display a dramatic change where the four-circulation balance status was broken. The flow field includes two main circulations and six small circulations at the corners and vertical centreline near the wall area. The flow field is excited to strong convection phenomena, even the temperature contours clearly demonstrating the strong convective patterns (see *Figure 10*). In fact, we can find other details from the point data history which shows that the velocity and temperature vary subharmonically with the forcing function. The averaged results shown here are obtained by averaging the data of one forcing cycle corresponding to half of the velocity cycle or temperature cycle. If we did the average by using the other half velocity cycle, the contours would be the same pattern but the eddies would appear at opposite locations symmetric to the horizontal centreline with the current pattern.

According to the above results, the first three cases are unexcited examples where the flow is a synchronous response; but the fourth is an excited and subharmonic response case. As the frequency is reduced, the strength of the circulation is increased. Here ω approaching 20 is the critical frequency range for flow transferring from a synchronous characteristic to a subharmonic characteristic.

The second set of computations is focused on horizontal gravity modulation effect which means the modulation direction is perpendicular to the temperature gradient direction. Like the terrestrial examples, the flow is more sensitive to the horizontal modulation effect. As in the previous procedure, the high frequency case is studied first in order to investigate the excitation frequency; and the other parameters are the same as vertical modulation cases. We started from $\omega = 450$ and listed the results in *Figure 11*. There are four counter-rotating circulations in the fluid domain. The lower left and upper right circulations are in clockwise direction but the other two in counter rotation. A conductive heat transfer pattern exists in temperature distribution. Both the velocity and temperature response are synchronous with the forcing function as evident from *Figure 11*. Because the conductive mechanism dominates the heat transfer phenomena, the time-averaged Nusselt number (defined as $-\partial\theta/\partial y$) along the hot wall is almost close to unity.

We continuously reduced the frequency to find the difference. The streamlines, isotherms and point data history are similar to $\omega = 450$ results, but the stream function values are increased.

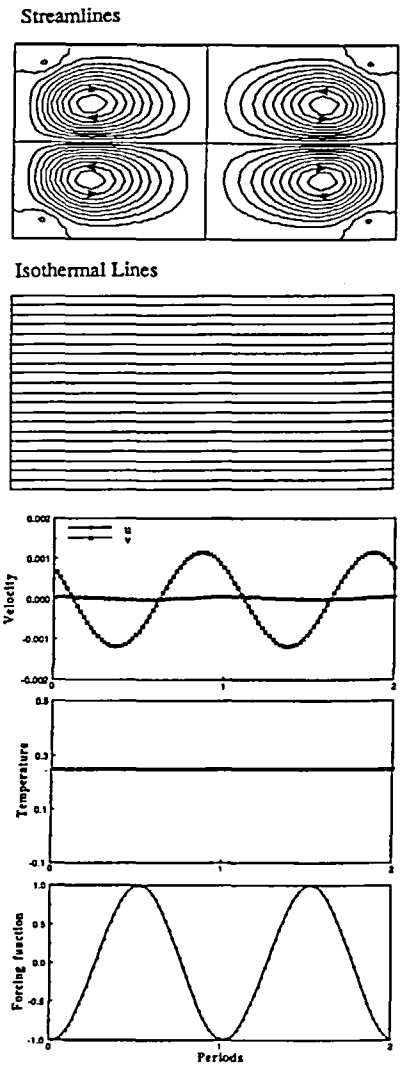

Figure 7 Time-averaged results for $Ra = 1.771 \times 10^5$, $Pr = 0.007$, $\eta = 1$, $\omega = 4543$, $Ar = 0.5$, zero-g (vertical jitter), ($\Psi_{max} = 0.0000035$, $\Psi_{min} = -0.0000035$, 19 contour lines), ($\theta_{max} = 0.5$, $\theta_{min} = -0.5$, 21 contour lines)

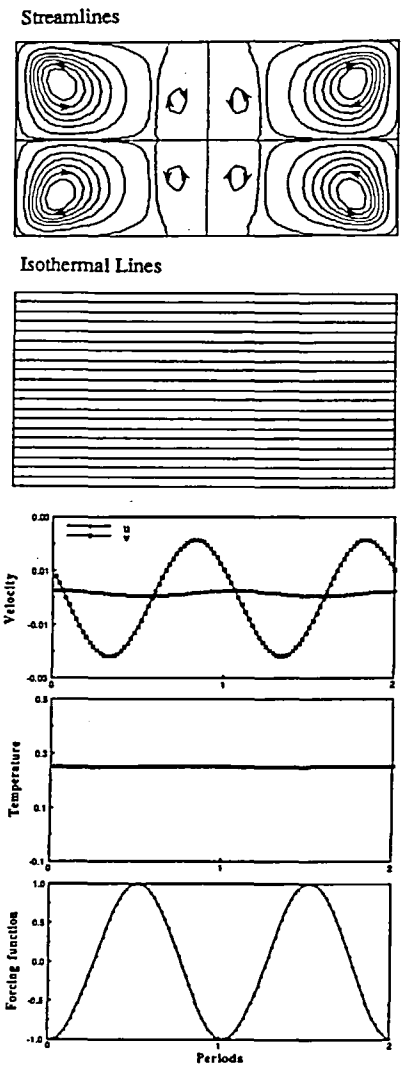

Figure 8 Time-averaged results for $Ra = 1.771 \times 10^5$, $Pr = 0.007$, $\eta = 1$, $\omega = 200$, $Ar = 0.5$, zero-g (vertical jitter), ($\Psi_{max} = 0.0007$, $\Psi_{min} = -0.0007$, 19 contour lines), ($\theta_{max} = 0.5$, $\theta_{min} = -0.5$, 21 contour lines)

When the frequency was diminished to $\omega = 200$, the flow started to be excited. In the fluid domain, there are a big clockwise circulation resulting from the combination of the two circulations existing in the upper right and the lower left portion in the previous case and two counterclockwise circulations shrinking small at the corners, as seen in *Figure 12*. The temperature distribution displays a small slope, the location of peak of the time-averaged Nusselt number moves to the right hand side, and the values become bigger because of the convective effect.

As the frequency is continuously decreased to 85, the flow field develops a strongly convective flow where small eddies start to appear in addition to the primary clockwise vortex (see *Figure*

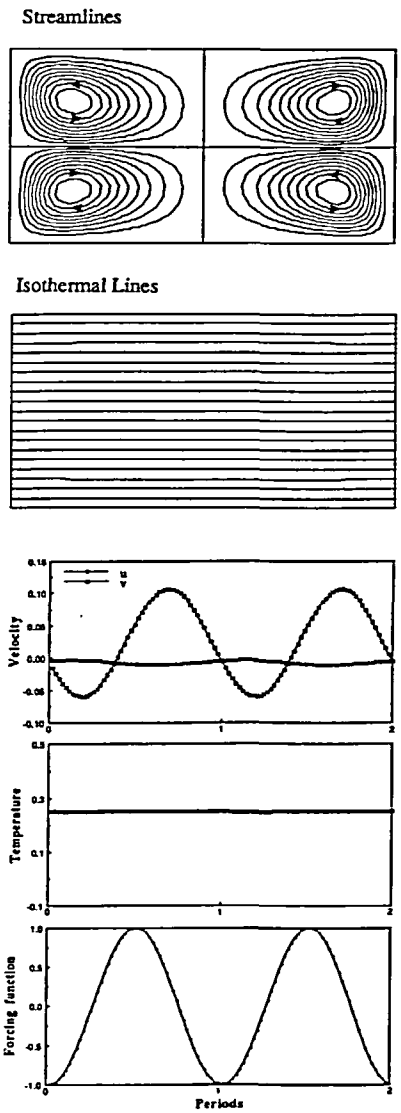

Figure 9 Time-averaged results for $Ra = 1.771 \times 10^5$, $Pr = 0.007$, $\eta = 1$, $\omega = 45.5$, $Ar = 0.5$, zero-g (vertical jitter), ($\Psi_{max} = 0.012$, $\Psi_{min} = -0.012$, 19 contour lines), ($\theta_{max} = 0.5$, $\theta_{min} = -0.5$, 21 contour lines)

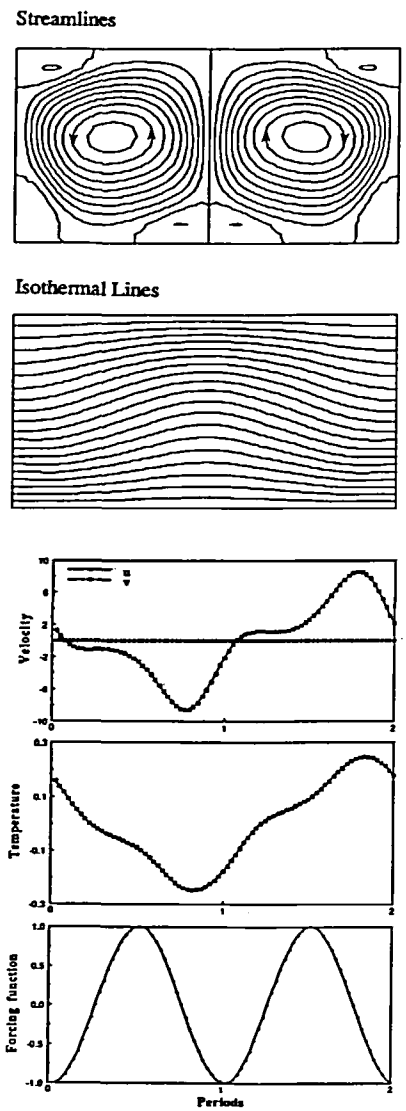

Figure 10 Time-averaged results for $Ra = 1.771 \times 10^5$, $Pr = 0.007$, $\eta = 1$, $\omega = 20$, $Ar = 0.5$, zero-g (vertical jitter), ($\Psi_{max} = 0.627$, $\Psi_{min} = -0.627$, 19 contour lines), ($\theta_{max} = 0.5$, $\theta_{min} = -0.5$, 21 contour lines)

13). The point data history shows deviation from the periodicity which is likely caused by the strong non-linear effect. The strongly excited flow distorts the temperature distribution and creates a high gradient which results in high Nusselt number values.

From the previous analyses, it is evident that a further reduction of ω will be interesting since a range of resonant frequencies for the cavity flow is being approached. Therefore, in *Figure 14*, the results of $\omega = 40$ case are listed. The point data history shows that the flow field displays strong deviations from sinusoidal response and the temperature contours demonstrate a strongly distorted pattern. The time-averaged results shown here are made by choosing an arbitrary

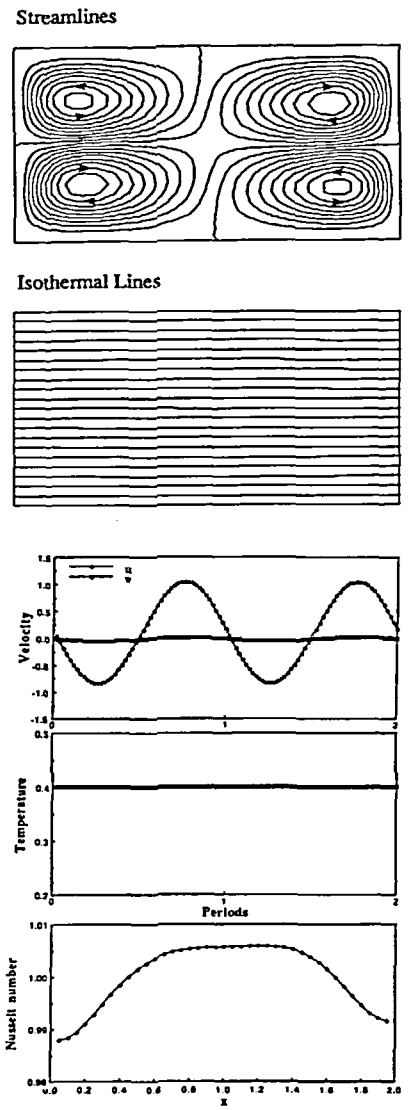

Figure 11 Time-averaged results for $Ra = 1.771 \times 10^5$, $Pr = 0.007$, $\eta = 1$, $\omega = 450$, $Ar = 0.5$, zero-g (horizontal jitter), ($\Psi_{max} = 0.027$, $\Psi_{min} = -0.032$, 19 contour lines), ($\theta_{max} = 0.5$, $\theta_{min} = -0.5$, 21 contour lines)

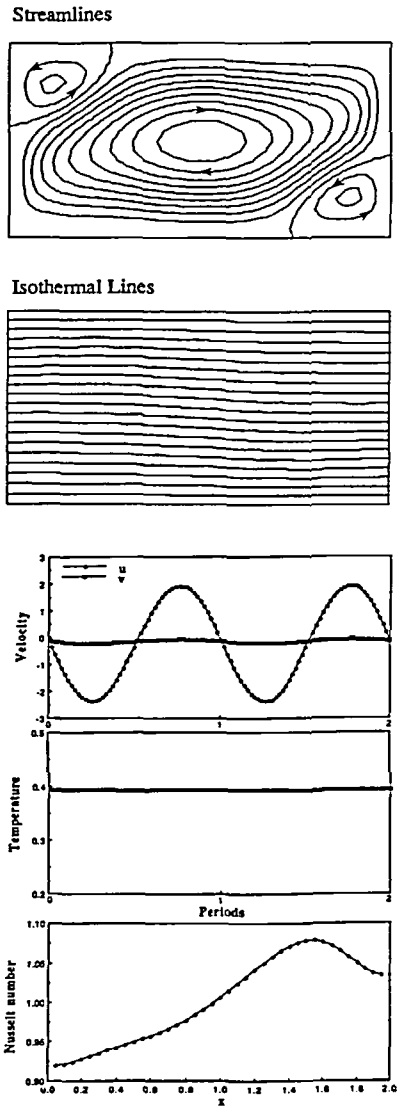

Figure 12 Time-averaged results for $Ra = 1.771 \times 10^5$, $Pr = 0.007$, $\eta = 1$, $\omega = 200$, $Ar = 0.5$, zero-g (horizontal jitter), ($\Psi_{max} = 0.057$, $\Psi_{min} = -0.245$, 12 contour lines), ($\theta_{max} = 0.5$, $\theta_{min} = -0.5$, 21 contour lines)

forcing function period, so it does not represent each cycle. The strong distortion is regarded as a consequence of the non-linear coupling of higher modes.

In summary, these examples investigated the horizontal modulation effect in zero-gravity to provide the critical frequency for the transformation from conduction to convection. In addition, due to the coupling of high mode excitation, the low frequency cases gradually behave deviations from sinusoidal point data history.

For further interest, the investigation of the effect of removing the gravity modulation from a modulated flow field was also explored. The final results of the horizontal modulation $\omega = 85$

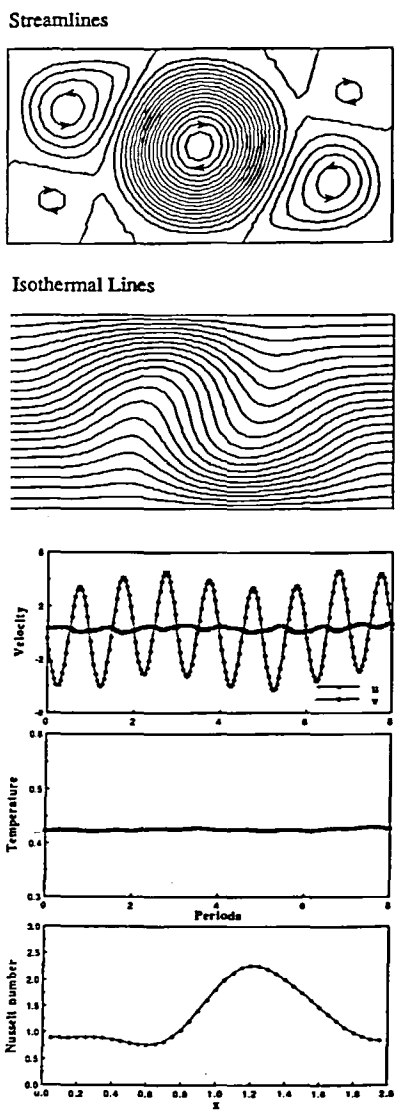

Figure 13 Time-averaged results for $Ra = 1.771 \times 10^5$, $Pr = 0.007$, $\eta = 1$, $\omega = 85$, $Ar = 0.5$, zero-g (horizontal jitter), ($\Psi_{max} = 0.91$, $\Psi_{min} = -3.34$, 25 contour lines), ($\theta_{max} = 0.5$, $\theta_{min} = -0.5$, 21 contour lines)

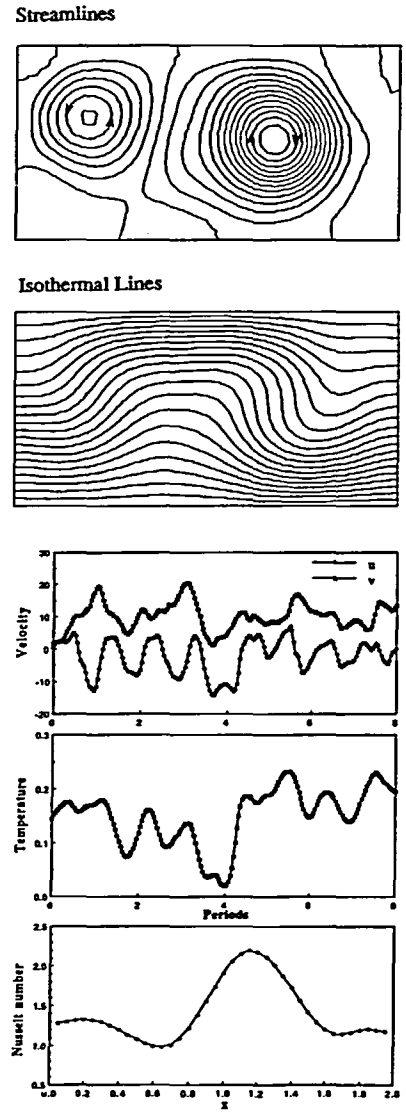

Figure 14 Time-averaged results for $Ra = 1.771 \times 10^5$, $Pr = 0.007$, $\eta = 1$, $\omega = 40$, $Ar = 0.5$, zero-g (horizontal jitter), ($\Psi_{max} = 2.24$, $\Psi_{min} = -4.29$, 19 contour lines), ($\theta_{max} = 0.5$, $\theta_{min} = -0.5$, 21 contour lines)

were selected as the initial condition for the calculation without a forcing function. In *Figure 15*, the point data history illustrates the velocity and temperature asymptotically approaching a steady constant value; and it is evident the temperature oscillations were damped much faster than the velocity, as is expected from the high heat diffusive nature of the low Pr materials. The flat isothermal contours and weak stream function values explain the system regressing to a conductive state.

Finally, a different Prandtl number case is conducted to understand the differences caused by Prandtl number. Similarly, the horizontal modulation $\omega = 85$ results were selected as a reference.

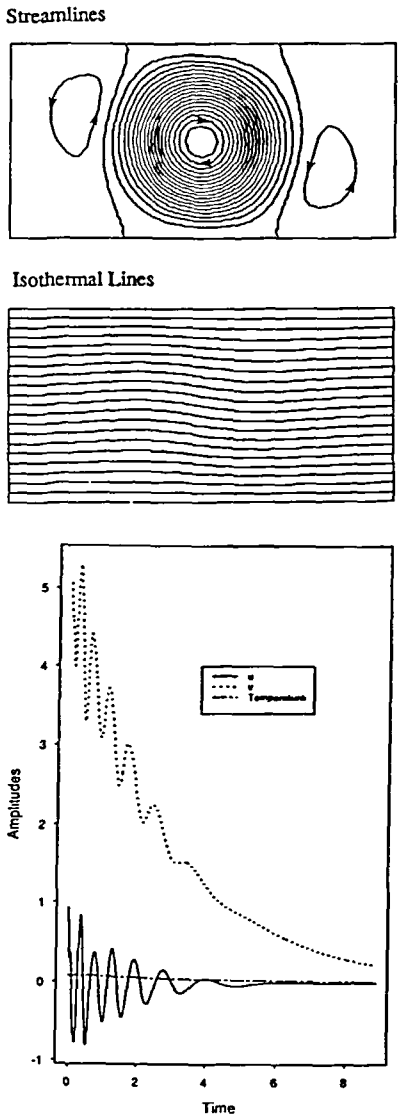

Figure 15 Time-averaged results for $Ra = 1.771 \times 10^5, Pr = 0.007, \eta = 85, \omega = 85\ Ar = 0.5$, zero-$g$ (horizontal jitter), ($\Psi'_{max} = 0.031$, $\Psi_{min} = -0.38$, 19 contour lines), ($\theta_{max} = 0.5$, $\theta_{min} = -0.5$, 21 contour lines)

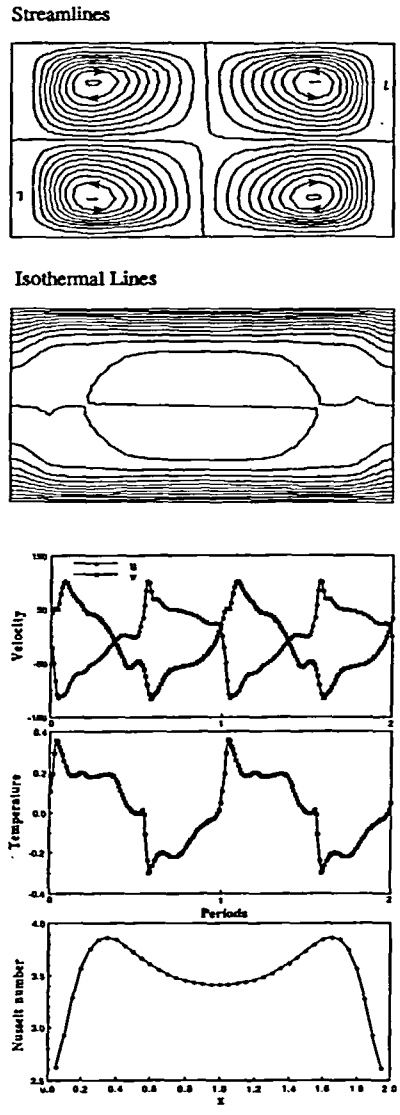

Figure 16 Time-averaged results for $Ra = 1.771 \times 10^5$, $Pr = 0.71$, $\eta = 1$, $\omega = 85$, $Ar = 0.5$, zero-g (horizontal jitter), ($\Psi_{max} = 3.65$, $\Psi_{min} = -3.65$, 19 contour lines), ($\theta_{max} = 0.5$, $\theta_{min} = -0.5$, 21 contour lines)

We changed the Pr to be 0.71 corresponding to the air property and kept the other parameters as the reference case. For this case (see *Figure 16*), the maximum value of the stream function occurs at an off-centre location in the cavity. The time-averaged results contain four circulations; and the strength of circulations are the same order, which is quite different from the reference case. The temperature field, as expected, is more excitatory than the low Prandtl number case. The point data history shows a strong non-linearity of the flow and the time-averaged Nusselt number displays a higher value according to the higher Prandtl number corresponding to the higher heat transfer rate.

CONCLUDING REMARKS

In this study, a rectangular cavity flow affected by sinusoidal gravity modulation in terrestrial and zero-gravity situations was successfully simulated by a semi-implicit projection finite element method. The stable phenomena with gravity modulation amplitudes frequency in the terrestrial condition were studied first. Then a parametric study of the effect of gravity modulation direction and frequency for zero-gravity environment was also included. Under these simulations, the sinusoidal gravity modulation indicated synchronous and subharmonic responses are in good agreement with Gresho and Sani's analyses.

In the zero-gravity conditions, it is a common in both vertical and horizontal modulation cases that the heat transfer mechanism transfers from conduction to convection along with the increase of vortex strength as the frequency diminishes. In the vertical modulation condition, the synchronous response exists in high frequency conductive states and gradually the convection enhances its effect resulting in the appearance of a subharmonic response with the decrease of frequency. On the other hand, instead of displaying the subharmonic response at low frequency, the horizontal modulation cases display deviations from sinusoidal point data response and create small eddies in the flow domain. Furthermore, the change of the Pr to the higher value exhibits an obviously different result from the low Pr case and forces all the eddies to be of same order.

In conclusion, this research provides information about the influence of gravity modulation effect in the fluid flow and heat transfer phenomena for a Benard convection. Following the broad applications of the Benard convection with gravity modulation in low-gravity crystal growth process, this study will benefit the understanding of this process. Furthermore, the investigation of the combination of gravity modulation in a thermal driven cavity flow with surface tension effect will be another important topic of research interest for the real simulation of crystal growth process.

REFERENCES

1 Gresho, P. M. and Sani, R. L. The effects of gravity modulation on the stability of a heat fluid layer, *Fluid Mech.*, **40**, 783 (1970)
2 Rappo, M. N., Davis, S. H. and Rosenblat, S. Benard convection with time-periodic heating, *Phys. Fluids*, **27**, 796 (1984)
3 Wang, C. Y. Generation of steady flow by an oscillatory acceleration and an oscillation wall temperature, *Int. Commun. Heat Mass Transfer*, **14**, 211 (1987)
4 Wheeler, A. A., McFadden, G. B., Murray, B. T. and Coriell, S. R. Convective stability in the Rayleigh–Benard and directional solidification problems: high-frequency gravity modulation, *Phys. Fluids (A)*, **3**, 2847 (1991)
5 Knabe, W. and Eilers, D. Low gravity environment in space lab, *Acta Astronautica*, **9**, 187 (1982)
6 Gershuni, G. Z. and Zhukhovitskiy, Y. M. Vibration-induced thermal convection in weightlessness, *Fluid Mech. Soviet Res.*, **15**, 63 (1986)
7 Danabasoglu, G. and Biringen, S. Computation of convection flow with g-jitter in rectangular cavities, *Ist Nat. Fluid Dynamics Congr., Cincinnati, AIAA Paper 88-3727* (1988)
8 Biringen, S. and Peltier, L. J. Numerical simulation of 3-D Benard convection with gravitational modulation, *Phys. Fluids (A)*, **2**, 754 (1990)
9 Ramaswamy, B., Jue, T. C. and Akin, J. E. Semi-implicit and explicit finite element schemes for coupled fluid/thermal problems, *Int. J. Num. Meth. Eng.*, **34**, 675 (1992)
10 Ramaswamy, B. and Jue, T. C. Some recent trends and developments in finite element analysis for incompressible thermal flows, *Int. J. Num. Meth. Eng.*, **35**, in press (1993)
11 Tritton, D. J. *Physical Fluid Dynamics*, 2nd Edn, Oxford Science Publications, New York (1988)
12 Goldhirsch, I., Pelz, R. B. and Orszag, S. A. Numerical simulation of thermal convection in a two-dimensional finite box, *J. Fluid Mech.*, **199**, 1 (1989)
13 Kirchartz, K. R. and Oertel, H. Jr. Three-dimensional thermal cellular convection in rectangular boxes, *J. Fluid Mech.*, **192**, 249 (1988)
14 Lee, S. and Dulikravich, G. S. Accelerated computation of viscous incompressible flows with heat transfer, *Num. Heat Transfer (B)*, **19**, 223 (1991)